MSDE

PAPER

View Article Online
View Journal | View Issue

Cite this: *Mol. Syst. Des. Eng.*, 2023, **8**, 1418

Isolating the effects of gate layer permeability and sorbent density on the performance of solute-selective polymeric ion pumps†

Jonathan Aubuchon Ouimet, Alexander W. Dowling and William A. Phillip *

The growing demand for solute selective separations necessitates the development of materials and processes capable of separating species of similar charge and size. Polymeric ion pumps, which are composite membranes composed of a gate layer situated on top of a sorbent layer, have the potential to address this opportunity. The gate and sorbent layers are designed to undergo changes in permeability and affinity, respectively, in response to an external stimulus. Subsequently, cyclic changes in the stimulus promote the selective transport of a target solute. Within this study, a mathematical model and numerical solver were developed to investigate the effect of the gate layer resistance on the performance of polymeric ion pumps. Notably, imperfect gate layers lead to solute diffusing back into the feed solution, reducing but not irrevocably hindering membrane performance. In the limit of high sorbent densities, the fraction of solute diffusing into the receiving solution is determined by the relative resistances of the gate and sorbent layers while the total flux of the target solute increases in proportion to the sorbent density. The analysis highlights that current materials possess the necessary properties to fabricate polymeric ions pumps with performances that exceed conventional membrane systems. Enhancing the performance of polymeric ion pumps will rely on identifying material combinations that respond coherently to rapidly changing stimuli.

Received 3rd May 2023,
Accepted 19th July 2023

DOI: 10.1039/d3me00073g

rsc.li/molecular-engineering

Design, System, Application

The increasing global population and transition toward electrified energy systems will require the recovery and reuse of critical minerals and nutrients. Here, the design of polymeric ion pumps, which are composite membrane systems that can isolate target solutes from complex milieus, is evaluated. Specifically, the influence of the gate layer permeability on the productive flux of target solute is examined. External stimuli are used to switch the gate layer between open and closed conformations. When open, the gate should offer minimal resistance to the diffusion of solute into the sorbent layer. When closed, the gate layer should direct the diffusion of solute into the downstream reservoir. However, perfectly-closed gate layers that are impermeable and direct all of the solute into the downstream reservoir are challenging to produce. The analysis reported here reveals that imperfect gate layers do not irrevocably hinder the performance of the polymeric ion pumps. Instead, the optimal system operating conditions shift to smaller duty cycles that reduce the time during which solute can diffuse back into the upstream feed reservoir. The analysis affirms that a wide range of stimuli responsive materials already possess the properties necessary to advance the experimental development of polymeric ion pumps.

1. Introduction

Solute-selective separations are needed to help alleviate the stress on natural resources, isolate therapeutic molecules, and remove emerging contaminants from water supplies.[1–4] As one example, the demand for lithium has grown in parallel to the electric vehicle industry and may surpass available supplies.[5] This emerging issue has prompted research into the recovery of lithium from produced water, geothermal brines, and seawater.[5,6] Likewise, end-of-life battery recycling could enable the recovery, rather than the disposal, of lithium and other valuable minerals.[7,8] Similarly, their exists opportunities to recycle resources dissolved in municipal and industrial wastewater.[9–11] For instance, the extraction of minerals and metals from industrial mines results in tailings that contain toxic metals and contaminants. While there is an environmental need to treat the runoff, the dissolved species (*e.g.*, copper, cobalt, and rare earth elements) can potentially be harvested and used.[12–15] Emerging technologies may enable the separation and purification of valuable resources from these feed streams.[8,16] However the broad range of target solutes and compositions of these waste streams emphasize the continued need for fit-for-purpose separation materials.[17,18]

Department of Chemical and Biomolecular Engineering, University of Notre Dame, Notre Dame, IN 46556, USA. E-mail: wphillip@nd.edu

† Electronic supplementary information (ESI) available. See DOI: https://doi.org/10.1039/d3me00073g

Membranes with solute-tailored selectivity provide an opportunity to meet the growing demand for solute-specific separations. In this regard, there is broad interest in manipulating membrane-solute interactions to promote single-specie selectivity in materials.[19] For instance, supported liquid membranes use a selective mobile carrier – suspended in an organic solvent – to reversibly complex and transport solute across the membrane.[20–22] Although the membranes are highly selective, the carrier can leak into the feed and stripping solutions, decreasing the performance.[23] One alternative is to covalently bond the carrier to the membrane matrix. While bound carriers enhance partitioning, strong interactions may impede the transport of solute.[24–26] One example is the addition of crown ethers within polymeric membranes. The selectivity of crown ethers is driven by the size of the cation relative to the crown ether cavity and the strength of the interaction is related to the decrease in free energy associated with forming the complex.[27,28] It was found that stronger interactions led to increased partitioning and lower salt diffusivities.[29] Interestingly, strong interactions can lead to selective separations through partition driven gating; here, molecules with greater partition coefficients preferentially enter a confined pore thereby preventing other molecules from entering and subsequently diffusing through the membrane.[30] Although engineering ligand-solute interactions is a promising route, it remains unclear how stability constants can be tuned to enhance solute partitioning without immobilizing species.[31]

Interestingly, some biological proteins facilitate transport by using energy to switch between distinct conformations that modulate interactions with the environment. Notably, the open/closed configuration and selective binding sites of biological ion pumps can be mimicked by stimuli responsive functionalities. Polymeric ion pumps are formed by merging a stimuli responsive gate and sorbent layer. Experimentally, it has been demonstrated that polymeric ion pumps increase the diffusive flux of target solutes by undergoing cyclic, conformational changes that result in time averaged concentration gradients that are larger than those that result from diffusive transport through noninteracting membranes.[32] In one conformation, solute freely diffuses past the gate layer and is adsorbed by a sorbent that possesses a high density of active sites. In the other conformation, the gate layer is closed, the sorbent releases the bound solute and the solute diffuses preferentially into the downstream receiving solution. Solute can be pumped across the membrane by oscillating between the two conformations. For systems with perfect gate layers, solute will only diffuse into the receiving solution. Yet experimental gate layers cannot reject 100% of solutes and a portion of the solute will diffuse back into the feed solution. As such, two questions emerge: Can imperfect gate layers be used to create polymeric ion pumps? If so, what properties must gate layers possess for polymeric ion pumps to efficiently transport solute?

This study aims to understand how the performance and operating conditions of polymeric ion pumps are affected by the permeability of the gate layer. To begin, a mathematical model is developed to capture the performance metrics that describe 'leaky' gate layers (*i.e.*, gate layers that do not reject 100% of solute). A numerical solver is then created and implemented to study the effect of imperfect gate layers on the transport of solute. This information is used to understand how system operating conditions can be changed to promote transport into the receiving solution by minimizing the diffusion of solute into the feed solution. We then explore whether deficiencies in the gate layer can be overcome by engineering the material properties of the sorbent, or if imperfect gate layers irrevocably hinder the performance of the system. Within this context, we assess whether current materials possess the properties necessary to fabricate polymeric ion pumps, and what further improvements will advance the materials.

2. Theory

The polymeric ion pumps studied here are composite materials composed of a stimuli-responsive gate layer situated on top of a responsive sorbent layer (Fig. 1A). The gate layer can "open" and "close" to modulate the permeability of solute. The sorbent layer adsorbs solute when the binding sites are active and releases solute when a stimulus changes the sites to their inactive conformation. The two layers are designed to work in concert such that the sorbent sites are active when the gate layer is open (*i.e.*,

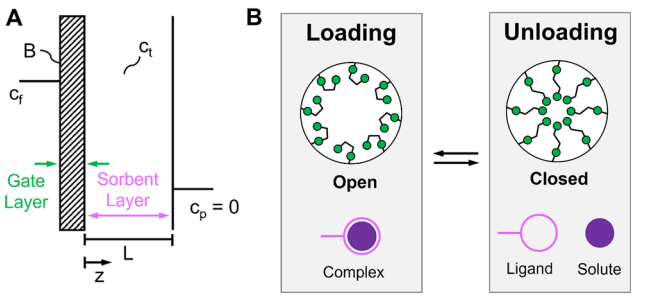

Fig. 1 Polymeric ion pumps rely on stimuli responsive gate and sorbent layers acting in concert to promote the selective transport of solute. (A) The sorbent layer has a predefined thickness, L, and density of active sites, c_t. The diffusion of solute in the sorbent is defined by the diffusion coefficient, D^s. The solute permeability coefficient, B, is a lumped parameter that captures the transport of solute through the gate layer. The feed solution, c_f, is well mixed. The downstream receiving solution, c_p, is absent of solute. (B) The gate and sorbent layers have two configurations. **Loading** – in the loading stage configuration, the gate layer is 'open' and allows solute to freely diffuse into the sorbent layer. The active sites of the sorbent layer instantaneously bind solute. **Unloading** – in the unloading stage configuration, the gate layer is 'closed' and the sorbent sites release the bound solute molecules. The diffusion of solute into the upstream feed solution is hindered by the gate layer. The ratio of the resistance offered by the sorbent layer relative to the gate layer is described by the Biot number, $\mathrm{Bi} = \frac{BL}{D^s}$.

loading stage) and inactive when the gate layer is closed (*i.e.*, unloading stage), Fig. 1B. The material properties of the two layers (*i.e.*, the density of active sites within the sorbent and permeability of the gate layer) and the system operating conditions (*i.e.*, the time spent in the loading and unloading stages) can be manipulated to achieve time averaged concentration gradients that are greater than those that result from steady-state diffusion. In turn, this increased driving force can be used to induce a preferential flux of target solute through the membrane.

2.1. Unloading stage: unsteady state mass balance

At the onset of the unloading stage, ligands within the sorbent layer release bound solute molecules and diffusion drives their transport out of the sorbent. The time dependent concentration profile of free solute in the sorbent layer can be determined by solving eqn (1).

$$\frac{\partial c^{s}}{\partial t} = D^{s}\frac{\partial^{2} c^{s}}{\partial z^{2}} \tag{1}$$

where c^{s} is the solute concentration and D^{s} is the diffusion coefficient of the solute in the sorbent layer, t is the time, and z defines the coordinate system across the thickness of the sorbent layer.

The effective function of the polymeric ion pumps requires that the density of sorbent sites be greater than the feed concentration.[32] Within this work, we consider the effect of an imperfect gate layer that allows solute to diffuse both upstream into the feed solution and downstream into the receiving solution during the unloading stage. This physical phenomenon is described using a boundary condition that quantifies the flux of solute at the interface between the gate and sorbent layers at $z = 0$, eqn (2). The left-hand side of the equation represents solute diffusion in the sorbent layer and the right-hand side of the equation quantifies the transport through the gate layer.

$$-D^{s}\left.\frac{\partial c^{s}}{\partial z}\right|_{z=0} = -B\left(c^{s}|_{z=0} - c_{f}\right) \tag{2}$$

$c^{s}|_{z=0}$ is the concentration of solute at interface between the gate and sorbent layers, c_{f} is the concentration of solute in the feed solution, and B is the solute permeability coefficient for the gate layer.[33] This form of the equation implies that the gate layer is at pseudo-steady state. The receiving solution, c_{p}, is assumed to be well mixed and free of solute, eqn (3).

$$c^{s}|_{z=L} = c_{p} = 0 \tag{3}$$

The initial condition, required to solve eqn (1) is defined by the concentration profile at the end of the previous loading stage, eqn (4).

$$\underbrace{c^{s}(z)|_{t_{ul}=0}}_{\substack{\text{start of}\\ \text{unloading}}} = \underbrace{c^{s}(z)|_{t=t_{l}}}_{\substack{\text{end of}\\ \text{loading}}} \tag{4}$$

The feed concentration and the thickness of the sorbent layer are used to non-dimensionalize the concentration of solute and the coordinate system, respectively. The diffusion time, $t_{D} = L^{2}/D^{s}$, emerges naturally to non-dimensionalize the time, eqn (5).

$$\mathbb{c} = \frac{c^{s}}{c_{f}}, \xi = \frac{z}{L}, \tau = \frac{t}{L^{2}/D^{s}} \tag{5}$$

As such, the governing equation, boundary conditions and initial condition are rewritten, eqn (6)–(9).

$$\frac{\partial \mathbb{c}}{\partial \tau} = \frac{\partial^{2}\mathbb{c}}{\partial \xi^{2}} \tag{6}$$

$$-\frac{\partial \mathbb{c}}{\partial \xi} = -\frac{BL}{D^{s}}\left(\mathbb{c}|_{\xi=0} - 1\right) = -\mathrm{Bi}\left(\mathbb{c}|_{\xi=0} - 1\right) \tag{7}$$

$$\mathbb{c}|_{\xi=1} = 0 \tag{8}$$

$$\mathbb{c}(\xi)|_{\tau_{ul}=0} = \mathbb{c}(\xi)|_{\tau=\tau_{l}} \tag{9}$$

The Biot number, Bi, appears in the upstream boundary condition (eqn (7)) due to the dimensional analysis. Physically, the Biot number represents a ratio of the resistance to permeation offered by the sorbent layer relative to the gate layer. For an impermeable gate layer, which offers infinite resistance, Bi = 0. If the gate layer offers a finite resistance, Bi > 0, and solute flows into the upstream solution. The larger the Biot number, the more easily solute can flow into the feed solution.

The derivation of and final solution for the unloading stage concentration profile is provided within the ESI.†

2.2. Loading stage: unsteady state mass balance

Upon switching to the loading stage, the permeability of the gate layer increases and the ligands within the sorbent layer take their active conformation. Within the sorbent layer, it is assumed that the solute left from the previous unloading stage is bound instantaneously by the active sites. Solute from the feed solution diffuses into the sorbent layer due to the concentration difference. Because the binding reaction is assumed to be instantaneous, the flux of solute is modeled as a reactive front that propagates through the sorbent layer, eqn (10).[34,35]

$$J = \frac{D^{s}}{\bar{L}}\left(c_{f} - 0\right) \tag{10}$$

J is the diffusive flux of solute and $\bar{L}$ is the thickness of the reactive penetration front.[36] For gate layers that do not impose a resistance to the flow of solute into the sorbent, as is assumed here, the concentration at the interface between the sorbent layer and the gate layer is equal to the feed concentration. Due to the instantaneous reaction assumption, the concentration of free solute past the penetration front is equal to zero.

At the beginning of the loading stage, the concentration profile of available binding sites, $c_{av}(z)$, is related to the ligand concentration, c_t, the solute remaining at the end of the prior unloading stage, $\underbrace{c^s(z)|_{t=t_{ul}}}_{\text{end of unloading}} = \underbrace{c^s(z)|_{t_l=0}}_{\text{start of loading}}$, and the stoichiometric ratio of ligands necessary to bind one solute molecule, $\mathfrak{v}$, eqn (11).

$$c_{av}(z) = c_t - \mathfrak{v}c^s(z)|_{t_l=0} \tag{11}$$

The concentration of available active sites is calculated with a mass balance, eqn (12).

$$\frac{d}{dt}\left(Ac_{av}\left[L-\bar{L}\right]\right) = -\mathfrak{v}JA \tag{12}$$

A is the membrane area and t_l is the loading time.

An expression describing the length of the penetration front with respect to time, eqn (13), is obtained by consolidating eqn (10)–(12) and recognizing that A and c_{av} do not depend on the time. As the loading stage progresses, the penetration front grows and the diffusive flux decreases.

$$\left(\frac{c_t}{\mathfrak{v}} - c^s|_{t_l=0}\right)\frac{d\bar{L}}{dt} = \frac{D^s}{\bar{L}}c_f \tag{13}$$

The effective density of sites, $\frac{c_t}{\mathfrak{v}}$, and the penetration front are non-dimensionalized with respect to the feed concentration and the thickness of the sorbent layer, eqn (14).

$$\mathbb{c}_x = \frac{c_t}{\mathfrak{v}c_f}, \ell = \frac{\bar{L}}{L} \tag{14}$$

For experimentally defined loading times, τ_l, the penetration front is calculated by integrating eqn (15).

$$\int_0^{\tau_l} d\tau = \int_0^{\ell} (\mathbb{c}_x - \mathbb{c}|_{\tau_l=0})\xi d\xi \tag{15}$$

The solute concentration profile at the end of the loading stage is defined by a piecewise function, eqn (16). At positions less than the penetration front, sorbent sites are saturated. At positions beyond the penetration front, the concentration of bound solute in the membrane is equal to the concentration of free solute from the previous unloading stage.

$$\mathbb{c} = \begin{cases} \mathbb{c}_x & \text{for } 0 < \xi \leq \ell \\ \underbrace{\mathbb{c}|_{\tau=\tau_{ul}}}_{\substack{\text{end of} \\ \text{unloading}}} = \underbrace{\mathbb{c}|_{\tau_l=0}}_{\substack{\text{start of} \\ \text{loading}}} & \text{for } \ell < \xi < 1 \end{cases} \tag{16}$$

2.3. Cycling leads to the emergence of a pseudo-steady state

A pseudo-steady state (PSS) emerges after cycling through the loading and unloading stages.[32] At pseudo-steady state, the total flux of solute into the sorbent layer is equal to the total flux of solute out. Quantifying the flux of solute over the course of a full period ($\tau_T = \tau_{ul} + \tau_l$), can be used to assess if the system is operating at pseudo-steady state.

During the unloading stage, solute diffuses out of the sorbent layer and into the feed and receiving solutions. The total solute that exits the membrane, $\mathcal{F}_{out}$, is calculated by integrating the flux at the sorbent layer boundaries (*i.e.*, $\xi = 0$ and $\xi = 1$) over the unloading stage time, eqn (17). The flow of solute into the membrane is equal to zero, $\mathcal{F}_{in}(\tau_{ul}) = 0$.

$$\mathcal{F}_{out}(\tau_{ul}) = \int_0^{\tau_{ul}} \left(-\frac{d\mathbb{c}}{d\xi}|_{\xi=0} + -\frac{d\mathbb{c}}{d\xi}|_{\xi=1}\right) d\tau_{ul} \tag{17}$$

During the loading stage, the solute that enters the membrane is obtained by integrating the number of available active sites over the length of the penetration front, eqn (18).

$$\mathcal{F}_{in}(\tau_l) = \int_0^{\ell} (\mathbb{c}_x - \mathbb{c}|_{\tau_l=0}) d\xi \tag{18}$$

It is assumed that solute does not diffuse into the receiving solution as long as the penetration front is smaller than the thickness of the sorbent matrix ($\mathcal{F}_{out}(\tau_l < \tau_{sat}) = 0$). Here, τ_{sat} is the time required for the penetration front to reach the interface between the sorbent layer and the receiving solution (*i.e.*, $\ell = 1$). Therefore, over the course of a period, the total solute that exits the membrane is given by

$$\mathcal{F}_{out} = \mathcal{F}_{out}(\tau_{ul}) = \int_0^{\tau_{ul}} \left(-\frac{d\mathbb{c}}{d\xi}|_{\xi=0} - \frac{d\mathbb{c}}{d\xi}|_{\xi=1}\right) d\tau_{ul} \tag{19}$$

and the total solute that enters the membrane is given by

$$\mathcal{F}_{in} = \mathcal{F}_{in}(\tau_l) = \int_0^{\ell} (\mathbb{c}_x - \mathbb{c}|_{\tau_l=0}) d\xi \tag{20}$$

At pseudo-steady state, eqn (19) and (20) can be equated, eqn (21).

$$\int_0^{\ell} (\mathbb{c}_x - \mathbb{c}|_{\tau_l=0}) d\xi = \int_0^{\tau_{ul}} \left(-\frac{d\mathbb{c}}{d\xi}|_{\xi=0} - \frac{d\mathbb{c}}{d\xi}|_{\xi=1}\right) d\tau_{ul} \tag{21}$$

Under these conditions, the concentration profiles of the loading and unloading stage are periodic and fully described by material properties (*i.e.*, Bi, $\mathbb{c}_x$) and system operating conditions (*i.e.*, τ_{ul}, τ_l). A useful metric to discuss the operating conditions is the duty cycle, the fraction of time spent in the unloading stage, eqn (22).

$$\text{Duty cycle} = \frac{\tau_{ul}}{\tau_{ul} + \tau_l} \quad (22)$$

2.4. Performance is defined relative to the diffusive flux

The performance, ψ, of polymeric ion pumps is quantified by normalizing the flow of solute into the receiving solution, $\mathcal{F}_{out}|_{\xi=1}$, with the flow of solute that occurs in a nonreactive system, $\mathcal{F}_{diffusive}$, eqn (23).[32] The flow through a nonreactive system is equal to the diffusive flow through a film with similar physical properties.

$$\psi = \frac{\mathcal{F}_{out}|_{\xi=1}}{\mathcal{F}_{diffusive}} = \frac{\mathcal{F}_{out}|_{\xi=1}}{\tau_l + \tau_{ul}} \quad (23)$$

The productive flux, ϕ, is a useful metric to examine the impact of a leaky, imperfect gate layer. The productive flux is defined as the fraction of solute that flows into the receiving solution relative to the total flow of solute out of the sorbent layer during the unloading stage, eqn (24). For systems with impermeable gate layers (Bi = 0), the productive flux of the system should be equal to 1. As the Biot number increases, it is hypothesized that the productive flux decreases.

$$\phi = \frac{\mathcal{F}_{out}|_{\xi=1}}{\mathcal{F}_{out}|_{\xi=1} + \mathcal{F}_{out}|_{\xi=0}} \quad (24)$$

3. Results and discussion

3.1. Validation of numerical solutions

The emergence of a pseudo steady state was validated by creating a numerical solver to iterate through the solutions of the solute flux during the loading and unloading stages. The solver is initialized with the material properties of the sorbent and gate layers (*i.e.*, $\mathbb{C}_x$, Bi), the loading and unloading times (*i.e.*, τ_{ul}, τ_l), and a solute concentration profile. Here, a fully saturated sorbent layer was used as the initial solute concentration profile, but as will be shown below, this choice is arbitrary. Once initialized, the integration constants for cycle 1 are calculated using a trapezoidal integration method with a sorbent layer discretized into 1001 finite elements. Subsequently, the membrane concentration profile at the end of the unloading stage was determined by applying eqn (S13)† to each finite element. The resulting unloading stage concentration profile was used to determine the concentration profile of available binding sites. The penetration front could then be evaluated from the concentration profile of available sites and user defined loading time, eqn (15). Subsequently, the loading stage concentration profile (eqn (16)) was used to calculate the integration constants for cycle 2. The numerical solver iterated through this process for 1000 cycles. The code used for the numerical solver is included within the ESI.†

Fig. 2 uses an initially saturated membrane to highlight the results of the numerical solver. Specifically, the concentration profiles at the end of the unloading and loading stages for 1, 5 and 100 cycles are presented. Fig. 2A and B correspond to systems where $\mathbb{C}_x$ = 10 and the Biot number is equal to 0 and 1, respectively. The black data points correspond to the unloading stage concentration profile after the first solver cycle. For a Bi = 0 system, the slope of the concentration profile is equal to or less than zero over the thickness of the sorbent layer. This curvature is indicative of solute diffusing into the receiving solution. On the other hand, for the Bi = 1 system, the concentration profile is parabolic. While solute still diffuses into the receiving solution, the positive slope of the concentration profile (*i.e.*, $\xi < 0.2$, for the first solver cycle) corresponds to the diffusion of solute into the upstream feed solution. In this model, the concentration of bound solute in the loading stage is a piecewise function. At positions less than or equal to the length of the penetration front (denoted by the black asterisk) the sorbent is saturated. At positions after the

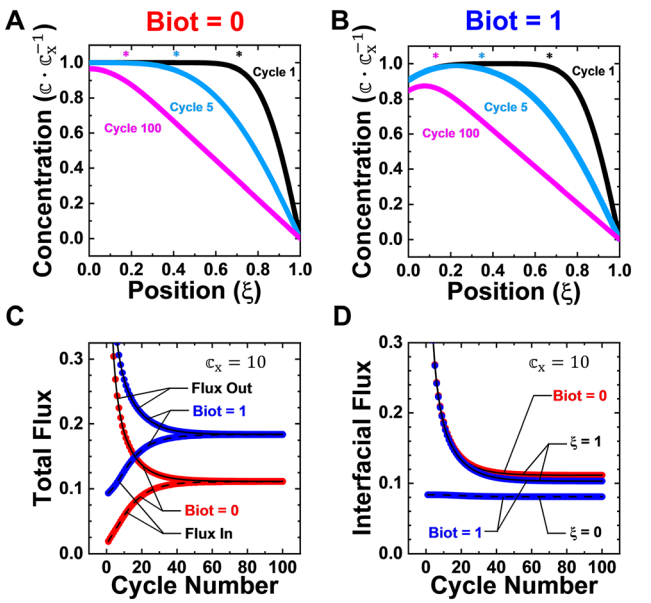

Fig. 2 Mathematical characterization of the approach to pseudo-steady state. Simulations are initialized with a saturated sorbent layer $\left(\frac{\mathbb{C}}{\mathbb{C}_x} = 1\right)$. The system shown here was operating at dimensionless unloading time, τ_{ul}, 0.01 and loading time, τ_l, 0.0125. The concentration profiles after 1, 5 and 100 unloading cycles are plotted for (A) Bi = 0 and (B) Bi = 1 systems. The location of the penetration fronts after 1, 5, and 100 cycles of the loading stage are indicated by the black, blue and magenta asterisks, respectively. (C) The total flux of solute entering (flux in) and exiting (flux out) the sorbent layer for the Bi = 0 (red data points) and Bi = 1 (blue data points) systems. (D) The interfacial components of the total flux out for Bi = 0 (red) and Bi = 1 (blue) systems. The data points indicated by ξ = 1 correspond to the flux of solute into the receiving solution. The data indicated by ξ = 0 corresponds to the flux of solute into the upstream reservoir. For an impermeable gate layer (*i.e.*, Bi = 0), solute does not flow into the upstream feed solution at ξ = 0.

penetration front (*i.e.*, $\xi > \ell$), the concentration of solute in the membrane is equal to that of the preceding unloading stage. The unloading stage profiles for cycle 5 and 100 are represented as blue and magenta data points, respectively. As the number of cycles increases, the excess solute provided by the initially saturated sorbent diffuses out and the concentration of solute in the membrane decreases. Thus, as the number of cycles increases from 1 to 5 to 100, the penetration front (black, blue, and magenta asterisks, respectively) decreases. The unloading and loading stage profiles for Bi = 0 and Bi = 1 are explicitly plotted in Fig. S1 and S2,† respectively. The concentration profiles are used to quantify the flux entering and exiting the membrane over the course of the loading and unloading stages.

Pseudo-steady state is achieved when the total flux of solute into the system is equal to the total flux out of the system. Fig. 2C shows that, for both the Bi = 0 and Bi = 1 systems, the total flux into and out of the polymeric ion pumps are equal after 60 cycles. Once PSS is reached, the unloading and loading stage concentration profiles are periodic. This is corroborated by a constant system performance and penetration front after 60 cycles of the solver iteration (Fig. S3†). Fig. 2D separates the unloading stage flux into the upstream (*i.e.*, $\xi = 0$) and downstream (*i.e.*, $\xi = 1$) components. For systems with an impermeable gate layer (Bi = 0, red data points) the solute flux is only into the downstream reservoir and the flux at $\xi = 0$ is always 0. These data points have been omitted from the figure. For systems with finite Biot numbers, there is an upstream and downstream component to the flux. These observations are consistent with the PSS concentration profiles (magenta data points) in Fig. 2A and B. The direction of the diffusional flux is determined by the local slope. For a Bi = 0 system, the derivative at $\xi = 0$ is equal to zero. Across the rest of the sorbent layer (*i.e.*, $\xi > 0$), the derivative is negative. This curvature is indicative of solute diffusing towards the receiving solution. On the contrary, for a Bi = 1 system, the concentration profile is parabolic. For instance, after 100 cycles, the slope of the Bi = 1 system is positive when $\xi < 0.08$ and negative when $\xi > 0.08$. Therefore, the diffusive flux is into both the upstream and downstream solutions.

Separating the total flux into the upstream and downstream components also highlights that the flux of solute into the receiving solution (indicated by the $\xi = 1$ marker) is greater for the Bi = 0 system. This finding is consistent with the physical intuition that an impermeable gate layer directs the solute into the receiving solution more effectively. For the Bi = 1 system, approximately half of the solute permeates into the downstream solution. This data is consistent with the definition of the Bi = 1 system where the resistance of the gate and sorbent layers, at $\xi = 0$, are equal.

The ESI† includes the solution for the Bi = 0 and Bi = 1 systems as they approach PSS from an initially empty membrane (Fig. S4†). For these systems, the change in the penetration front and performance are outlined in Fig. S5.† After cycling, both initial conditions lead to the same pseudo-steady state concentration profiles and fluxes. Having confirmed that the numerical solver approaches a pseudo-steady solution enables its use in elucidating the effect of material properties on system performance and operating conditions.

3.2. Imperfect gate layers decrease the performance of systems

The results of the solver routine developed here are in good agreement with a previously developed analytical solution. For

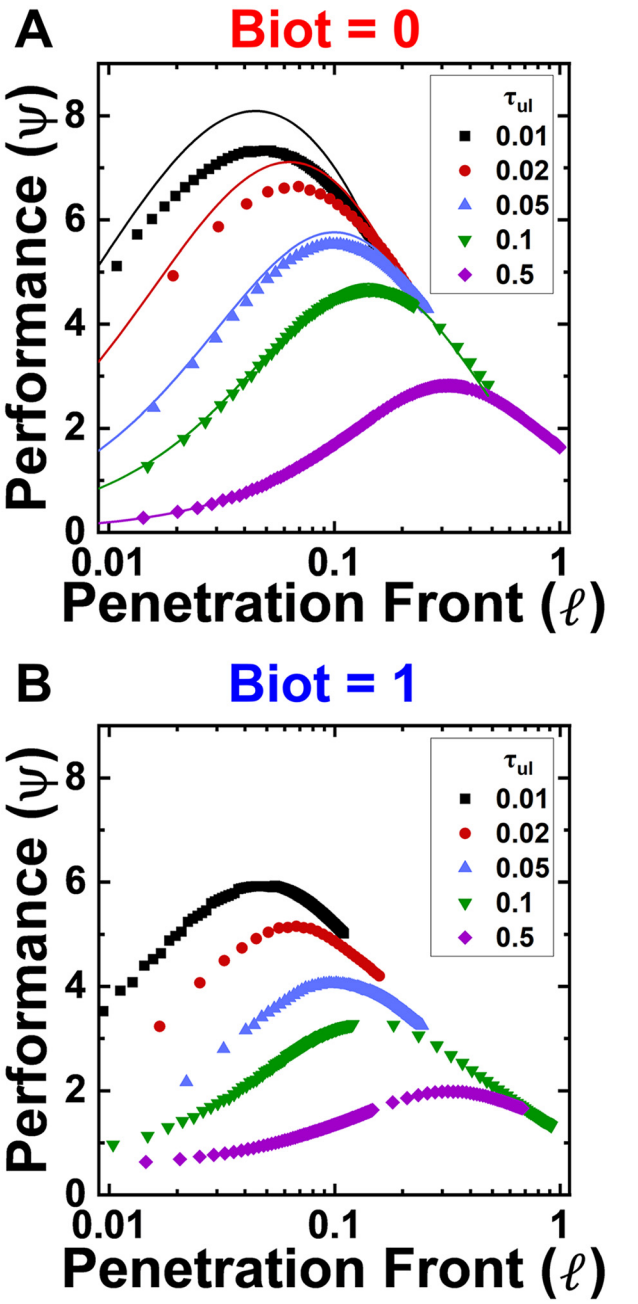

Fig. 3 The effect of the Biot number and system operating conditions on performance. For select unloading times, the performance of systems with $\mathbb{C}_x = 10$ and (A) Bi = 0 or (B) Bi = 1 are plotted with respect to the penetration front. The data points correspond to the performance of the system calculated with the numerical solver. For systems where (A) Bi = 0, the analytical solution is represented by the solid lines.[32]

a series of unloading times, Fig. 3A compares the performance as a function of the penetration front for a system where $\mathbb{C}_x$ = 10 and Bi = 0. Increasing the penetration front corresponds to an increase in the loading time. The performance is examined with respect to the penetration front and not the loading time because the optimal penetration front is uniquely defined for an unloading time and is independent of the Biot number (Fig. S6†). In contrast, at a fixed unloading time, the optimal loading time depends on the value of the Biot number and sorbent density. Within Fig. 3A, the performance of systems obtained from the numerical solver and analytical solutions are represented by data points and solid lines, respectively. The analytical predictions were validated experimentally with a system operating at τ_{ul} values that ranged from 0.03 to 0.4.[32] We suspect that the discrepancy between the analytical and the numerical solutions in the limit of fast switching is the result of simplifying assumptions underlying the analytical solution.

For each unloading time, there exists a penetration front that optimizes the system performance. For systems operating at a constant unloading time, the performance of the membrane is represented by a bell-shaped curve. For instance, at τ_{ul} = 0.05 (Fig. 3A, light blue triangles), the performance of the system initially increases as the penetration front increases from 0.01 to 0.1 and then decreases as the penetration front increases from 0.1 to 1. This parabolic curvature implies that for a select unloading time, there exists one loading time that optimizes the performance. As the unloading time is decreased, the optimal penetration front decreases and the performance of the system increases because the solute has a shorter distance to diffuse during the loading stage. This data implies that the performance of systems can be improved by designing gate and sorbent layers capable of oscillating rapidly between the loading and unloading stages.

The numerical solver allows a solution to be developed for systems with an imperfect gate layer (Bi > 0). Fig. 3B presents performance *vs.* penetration front curves for a system where $\mathbb{C}_x$ = 10 and Bi = 1. Even though the Biot number is increased, the general curvature of the data points remains the same. Additionally, the performance of the system is maximized in the limit of fast switching (τ_{ul}, $\ell \rightarrow 0$). This implies that changing the permeability of the gate layer does not change the fundamental operation of the system. Albeit, increasing the Biot number decreases the performance of the system. For instance, at τ_{ul} = 0.01, the optimal performance of the system decreases from 7.3 (Fig. 3A, black circles) to 5.9 (Fig. 3B, black circles). The decrease in performance is attributed to an increase in the flow of solute into the upstream feed solution.

The optimal operating conditions can be used to compare systems with different material properties. The performance of optimized systems with $\mathbb{C}_x$ = 10, 10^2 or 10^3 and Bi = 0, 0.1 or 1 at a variety of unloading times are compared in Fig. 4. A parity plot highlights the close agreement between the analytical (black lines) and numerical solutions (orange data points) for the Bi = 0 systems (Fig. S7†). For all systems, the

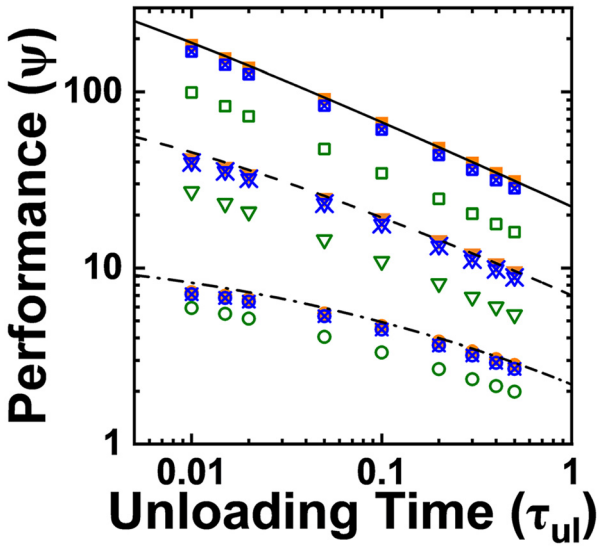

Fig. 4 The performance of systems with varying material properties. The dot-dash, dash and solid lines correspond to the analytical solution of systems with Bi = 0 and $\mathbb{C}_x$ = 10, 10^2, 10^3, respectively. Numerical solutions are represented by individual data points. Systems with $\mathbb{C}_x$ = 10, 10^2, 10^3 are represented by circles, triangles and squares respectively. The orange, blue and green data points correspond to systems where Bi = 0, 0.1 and 1, respectively.

performance increases with decreasing unloading times and decreasing Biot numbers.

3.3. Material properties effect the optimal system operating conditions

The duty cycle is a useful metric to understand the relationship between material properties and the optimal system operating conditions (Fig. 5). At constant $\mathbb{C}_x$ values, increasing the penetration front leads to a decrease in the duty cycle. Take the Bi = 0 and $\mathbb{C}_x$ = 10 (analytic solution – orange line, numerical solution – orange circular data points) system as an example. As the penetration front approaches zero, the time required for a solute to diffuse an infinitesimally small distance into the sorbent layer also approaches zero. The infinitesimally small diffusion distance corresponds to the loading time approaching 0 and, consequently, the duty cycle (eqn (22)) approaching $\frac{\tau_{ul}}{\tau_{ul}} = 1$ (Fig. S8†). As the penetration front approaches 1, $\tau_l \rightarrow \tau_{ul}$ and the duty cycle converges to 50%. Comparisons between systems can also be made across sorbent densities at constant penetration fronts. For instance, when the sorbent density is increased from 10 to 1000 (orange and green data, respectively) the duty cycle decreases. For sorbents with a high density of active sites, the duty cycle will converge to 50%. An increase in the sorbent density results in a larger number of open binding sites between the interface at ξ = 0 and the penetration front. The relationship between the total ligand density and the number of available binding sites was established in eqn (11). Therefore, at a constant penetration front, the increase in available sites corresponds to an

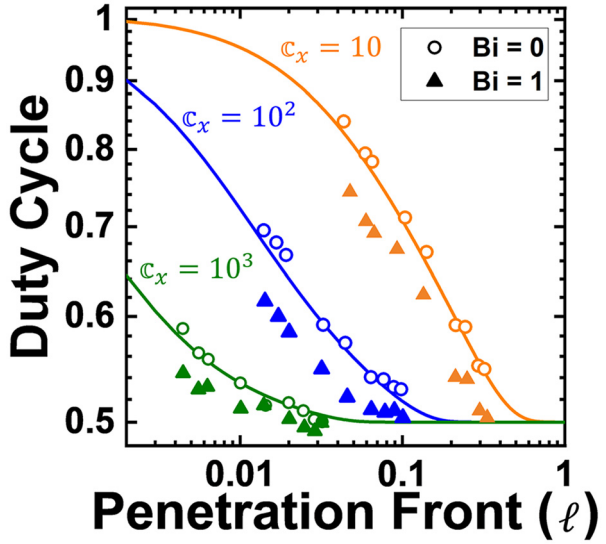

Fig. 5 The optimal process operating conditions (*i.e.*, τ_{ul} and τ_l) converge with increasing sorbent densities. The solid lines correspond to the analytical solutions of systems with impermeable gate layers and sorbent densities of 10 (orange), 100 (blue) and 1000 (green). For each sorbent density, open circles and filled triangles correspond to the numerical solution of systems with Biot numbers of 0 and 1, respectively.

increase in the loading time (eqn (15)) and, consequently, a decrease in the duty cycle.

At a constant sorbent density, the value of the duty cycle decreases as the Biot number increases. Fig. S6† highlights that at a constant penetration front, increasing the Biot number does not affect the unloading time. Therefore, the reduction in the duty cycle corresponds to the loading time increasing and the system spending a smaller fraction of time in the unloading stage. The loading time increases due to the increase in available binding sites with increasing Biot numbers. An alternative view point, is that the smaller duty cycle aims to minimize the loss of solute diffusing into the upstream feed solution during the unloading stage.

3.4. At sufficiently high $\mathbb{C}_x$ values, the total flux increases in proportion to the sorbent density

Isolating the influence of the Biot number and sorbent density on the performance of polymeric ion pumps provides information that can be used to guide future research into these membranes. Fig. 4 compared the performance of systems with $\mathbb{C}_x$ = 10, 10^2 or 10^3 and Bi = 0, 0.1 or 1. While increasing the Biot number always decreases the system performance, systems with greater sorbent densities experience a larger decrease in performance. For instance, at τ_{ul} = 0.1, the performance of systems where $\mathbb{C}_x$ = 10 (circle data points) decreases from 4.6 to 3.3 as the Biot number is increased from 0 to 1. On the other hand, the performance of systems where $\mathbb{C}_x$ = 10^3 (square data points) decreases from 61.1 (Bi = 0) to 34.4 (Bi = 1).

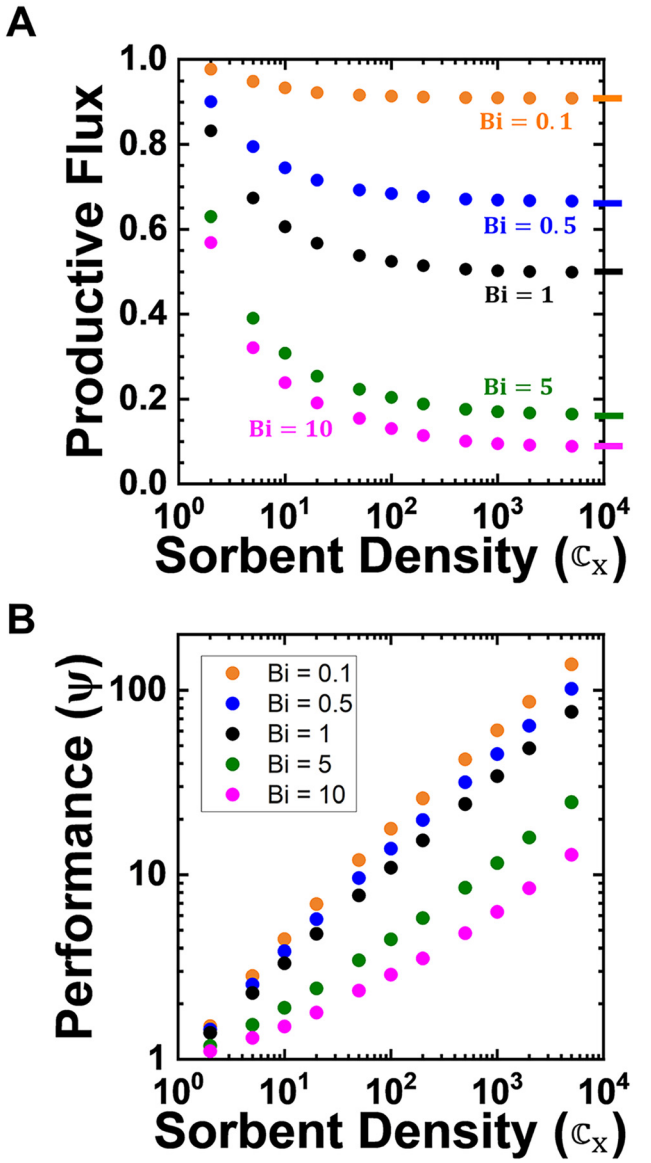

Fig. 6 For an optimized system running at τ_{ul} = 0.1, the (A) productive flux and the (B) performance is plotted at varying sorbent densities for five different Biot numbers. For (A), the dashed lines at $\mathbb{C}_x$ = 10^4 corresponds to the productive flux of a systems whose sorbent acts like a perfect sink.

Polymeric ion pumps with higher density sorbent layers experience a larger decrease in performance at finite Biot values because a larger fraction of solute diffuses into the upstream solution. Fig. 6A presents the productive flux of optimized systems operating at τ_{ul} = 0.1 for a variety of sorbent densities. In the limit that the sorbent density approaches 1, the concentration of solute at the interface between the gate and sorbent layer are equal. Consequently, there is no longer a driving force for solute to the diffuse into the feed solution and the productive flux converges to 1. At low and intermediate $\mathbb{C}_x$ values the productive flux decreases. Interestingly, at sufficiently high sorbent densities ($\mathbb{C}_x$ ~ 10^2), the productive flux approaches an asymptotic value. For

instance, increasing the sorbent density from 10^2 to 10^4 will only decrease the productive flux by 0.5% and 2.5% for the Bi = 0.1 and Bi = 1 systems, respectively. In the limit that $\mathbb{C}_x \rightarrow \infty$, the productive flux converges to a constant value of $\frac{1}{\mathrm{Bi}+1}$. This limit is represented by the hash marks at 10^4 in Fig. 6A.

A resistance in parallel analysis can be used to rationalize the values that the productive flux converges to in the limit of high-density sorbents. As the sorbent density increases, the penetration front approaches 0 (Fig. S9†). Physically, this corresponds to most of the solute being located at the interface between the gate and the sorbent layer at the outset of the unloading stage. In this limit, the productive flux is defined by the relative resistances of the gate, $\frac{1}{B}$, and sorbent, $\frac{L}{D}$, layers. Specifically, the fraction of solute diffusing into the permeate is equal to the resistance of the sorbent layer relative to the total resistance, eqn (25).

$$\frac{\mathcal{F}_{\mathrm{out}}\big|_{\xi=1}}{\mathcal{F}_{\mathrm{out}}\big|_{\xi=0}+\mathcal{F}_{\mathrm{out}}\big|_{\xi=1}}=\frac{D/L}{B+D/L}=\frac{1}{\mathrm{Bi}+1} \tag{25}$$

While the productive flux asymptotes at sufficiently high $\mathbb{C}_x$ values, the performance continues to increase in proportion to the sorbent density (Fig. 6B). The performance curves in Fig. 6B possess distinct behaviors depending on whether $\mathbb{C}_x$ is greater or less than $\sim 10^2$. Below sorbent densities of 10^2, the curves are concave if Bi < 1 and convex if Bi > 1. This distinct curvature indicates that when Bi < 1, incremental increases in the sorbent density improves the performance more relative to systems where Bi > 1. At sorbent densities greater than 10^2, the performance continues to increase and the curves appear to be parallel with one another. This trend is attributed to the productive flux no longer decreasing. At sufficiently high sorbent densities the effect of the Biot number and the sorbent density are deconvoluted. Specifically, the Biot number influences the relative spacing between the curves and the slope is defined by a power law dependence on the sorbent density, $\sim \mathbb{C}_x^{0.5}$.

3.5. Polymer materials that can mimic biological ion pumps exist

Using experimental data reported for pH responsive polymeric ion pumps, the measured performances were compared with those provided by the numerical solver.[32] The experimental system was composed of an amine-functionalized copolymer gate layer and an iminodiacetic acid sorbent. At low pH, the gate layer was protonated to form charged ammonium moieties that hindered the permeation of cations (*i.e.*, Ca^{2+}). At high pH, the amines within the gate layer were deprotonated (neutral) and ions could permeate into the underlying sorbent layer. For this system, the solute permeability coefficient was estimated as B = 0.21 μm s^{-1}.[37,38] The sorbent density ($\mathbb{C}_x \cong 2.6$), the diffusion coefficient (D_{eff} = 1.04 × 10^{-11} m^2 s^{-1}), the thickness of the membrane (L = 240 μm), and operating conditions (condition 1: t_l = 196 s, t_{ul} = 39 s and condition 2: t_l = 525 s, t_{ul} = 281 s) were reported within ref. 32. These values were used to determine τ_{ul}, τ_l, and the Biot number. A parity plot comparing the experimental and numerical performances is presented in Fig. S10.† For both operating conditions, the mathematical model aligns well with experimentally determined performances. As expected, relative to previous models that assumed a perfect gate layer (red squares), accounting for an imperfect gate layer (green circles) improves the prediction. Specifically, for a perfect gate layer, the numerical performances are always greater than the experimental performances because the model assumptions provide the numerical simulations with the advantage. Incorporating an imperfect gate layer accounts for solute loss to the feed solution during the loading phase. Further closing the gap between the experimental and theoretical predictions will require relaxing additional assumptions.

Advances in polymer science and engineering have resulted in a wealth of stimuli responsive materials that can be used as gates and sorbents. For instance, triblock copolymers can possess binding capacities as high as 4.1 mmol g^{-1} (2600 mmol L^{-1}).[39] For feed concentrations less than 26 mM, these capacities correspond to $\mathbb{C}_x$ values greater than 100. Additionally, hierarchically structured sorbents with nanoscale pores and microscale channels possess site densities greater than 250 mmol L^{-1}.[40] While the density of these sorbents are lower, the design of the structure provides higher diffusion coefficients and, consequently, smaller Biot numbers. Many other high-density sorbents that can reach $\mathbb{C}_x > 100$ exist.[41–44] With respect to gate layers, a variety of mechanisms (*e.g.*, steric hinderance, Donnan exclusion) have been designed to hinder solute transport. For instance, in addition to the charge phenomena described in the example above, pH responsive polymers can swell and collapse to enable nanopores to mimic the open and closed configurations of ion pumps.[45] Similarly, the cis/trans configurations of a light responsive azobenzene molecules can provide a physical barrier to diffusing solute.[46] These materials, and many others, possess permeabilities that correspond to Bi ≅ 0.1.[37,47–49]

The Biot number can also be manipulated by changing the relative thickness of the sorbent and gate layers. Specifically, the Biot number decreases proportionally to the thickness of the sorbent layer. Likewise, increasing the thickness of the gate layer decreases the solute permeability coefficient (*i.e.*, $B=\frac{\mathrm{DH}}{L}$) and consequently the Biot number. Although this is so, increasing the gate layer thickness will introduce resistance to solute diffusing into the sorbent during the loading stage. The effect of this loading stage resistance on performance is left to future work. As such, the performance of polymeric ion pumps will improve by understanding the physical constraints that the gate and

sorbent layer impose and, as suggested by the above analyses, developing materials that possess tunable, and rapid response to stimuli.[50] Therefore, systems that enable the rapid introduction of changes within the polymer on time scales consistent with the loading and unloading times are desired. In this regard, stimuli that can be introduced directly to the polymer, bypassing the need to change the surrounding solution environment, may enable faster reponses.[51] Therefore, we see light and electroactive polymer[52] materials are interesting avenues to explore.

4. Conclusion

The performance of polymeric ion pumps can be refined by developing better gate layers or creating higher density sorbents. The two layers improve the performance of polymeric ion pumps through distinct mechanisms. Improving the gate layer increases the productive flux of a system by directing a larger fraction of solute into the receiving solution. On the other hand, higher density sorbents increase the solute concentration gradient across the sorbent layer, which consequently, drives larger diffusive fluxes into the receiving solution. Within this work, a mathematical model and numerical solver were developed to deconvolute the effect of the gate and sorbent layers on the performance of polymeric ion pumps. The resistance of the gate and sorbent layers were related using the Biot number. For systems where the gate layer offers an infinite resistance, Bi = 0 and solute only flows into the receiving solution. For gate layers that offer a finite resistance, Bi $>$ 0 and solute flows into the both the receiving and feed solution during the unloading phase. For systems with imperfect gate layers, the optimal operating conditions shift to minimize the loss of solute during the unloading stage. Specifically, systems with larger Biot numbers spend a smaller fraction of time in the unloading stage and operate at lower duty cycles. Additionally, an increase in the Biot number leads systems with greater sorbent densities to experience larger decreases in performance. This is due to a larger fraction of solute diffusing into the upstream feed solution. The decrease in the performance can be overcome by tailoring the sorbent design. Specifically, at sufficiently high sorbent densities ($\mathfrak{C}_x \sim 10^2$), the fraction of solute diffusing into the receiving solution becomes defined by the relative resistance of the gate and sorbent layers, while the total flux continues to increase with the density of the sorbent. The model presented here sheds valuable insight on the design of sorbent and gate layers that create polymeric ion pumps in which the time averaged concentration gradients are greater than conventional membranes that rely on diffusive transport.

Nomenclature and variables

Dimensional variables

A Membrane area, m^2
B Solute permeability coefficient (gate layer), cm s^{-1}
c_{av} Available site concentration (sorbent layer), mol L^{-1}
c_f Feed concentration, mol L^{-1}
c_p Receiving solution concentration, mol L^{-1}
c^s Solute concentration in sorbent, mol L^{-1}
c_t Total ligand density (sorbent layer), mol L^{-1}
D^s Diffusion coefficient (sorbent layer), cm^2 s^{-1}
J Diffusive solute flux, mol m^{-2} s
L Thickness (sorbent layer), m
$\bar{L}$ Position of penetration front, m
t Time, s
t_l Loading Time, s
t_{ul} Unloading Time, s
z Position, m

Dimensionless variables

Bi Biot Number
$\mathfrak{C}$ Solute concentration
$\mathfrak{C}_x$ Sorbent density
$\mathcal{F}$ Flow
ℓ Penetration front position
$\mathfrak{v}$ Stoichiometric coefficient
ξ Position
τ Time
τ_l Loading time
τ_T Period length
τ_{ul} Unloading time
ϕ Productive flux

Conflicts of interest

There are no conflicts to declare.

Acknowledgements

This work was kindly support by the National Science Foundation (NSF) through award CBET 2147605. J.A.O. gratefully acknowledges support from the CEST/Bayer Predoctoral Fellowship.

References

1 D. S. Sholl and R. P. Lively, Seven Chemical Separations to Change the World, *Nature*, 2016, **532**(7600), 435–437, DOI: **10.1038/532435a**.
2 M. Ateia, A. Alsbaiee, T. Karanfil and W. Dichtel, Efficient PFAS Removal by Amine-Functionalized Sorbents: Critical Review of the Current Literature, *Environ. Sci. Technol. Lett.*, 2019, **6**(12), 688–695, DOI: **10.1021/acs.estlett.9b00659**.
3 A. L. Zydney, Membrane Technology for Purification of Therapeutic Proteins, *Biotechnol. Bioeng.*, 2009, **103**(2), 227–230, DOI: **10.1002/bit.22308**.
4 M. G. Jabra, C. J. Yehl and A. L. Zydney, Multistage Continuous Countercurrent Diafiltration for Formulation of Monoclonal Antibodies, *Biotechnol. Prog.*, 2019, **35**(4), e2810, DOI: **10.1002/btpr.2810**.

5 C. B. Tabelin, J. Dallas, S. Casanova, T. Pelech, G. Bournival, S. Saydam and I. Canbulat, Towards a Low-Carbon Society: A Review of Lithium Resource Availability, Challenges and Innovations in Mining, Extraction and Recycling, and Future Perspectives, *Miner. Eng.*, 2021, **163**, 106743, DOI: **10.1016/j.mineng.2020.106743**.

6 T. Investing, *The Lithium Boom - An Analysis Of Future Demand Vs. Supply| Seeking Alpha*, **https://seekingalpha.com/article/3984654-lithium-boom-analysis-of-future-demand-vs-supply**, (accessed 2023-02-27).

7 S. Kim, J. Kim, S. Kim, J. Lee and J. Yoon, Electrochemical Lithium Recovery and Organic Pollutant Removal from Industrial Wastewater of a Battery Recycling Plant, *Environ. Sci.: Water Res. Technol.*, 2018, **4**(2), 175–182, DOI: **10.1039/C7EW00454K**.

8 N. P. Wamble, E. A. Eugene, W. A. Phillip and A. W. Dowling, Optimal Diafiltration Membrane Cascades Enable Green Recycling of Spent Lithium-Ion Batteries, *ACS Sustainable Chem. Eng.*, 2022, **10**(37), 12207–12225, DOI: **10.1021/acssuschemeng.2c02862**.

9 R. M. DuChanois, N. J. Cooper, B. Lee, S. K. Patel, L. Mazurowski, T. E. Graedel and M. Elimelech, Prospects of Metal Recovery from Wastewater and Brine, *Nat. Water*, 2023, **1**(1), 37–46, DOI: **10.1038/s44221-022-00006-z**.

10 J. S. Guest, S. J. Skerlos, J. L. Barnard, M. B. Beck, G. T. Daigger, H. Hilger, S. J. Jackson, K. Karvazy, L. Kelly, L. Macpherson, J. R. Mihelcic, A. Pramanik, L. Raskin, M. C. M. Van Loosdrecht, D. Yeh and N. G. Love, A New Planning and Design Paradigm to Achieve Sustainable Resource Recovery from Wastewater, *Environ. Sci. Technol.*, 2009, **43**(16), 6126–6130, DOI: **10.1021/es9010515**.

11 D. Puyol, D. J. Batstone, T. Hülsen, S. Astals, M. Peces and J. O. Krömer, Resource Recovery from Wastewater by Biological Technologies: Opportunities, Challenges, and Prospects, *Front. Microbiol.*, 2017, **7**, 2106, DOI: **10.3389/fmicb.2016.02106**.

12 B. Mwewa, M. Tadie, S. Ndlovu, G. S. Simate and E. Matinde, Recovery of Rare Earth Elements from Acid Mine Drainage: A Review of the Extraction Methods, *J. Environ. Chem. Eng.*, 2022, **10**(3), 107704, DOI: **10.1016/j.jece.2022.107704**.

13 B. Rezaie and A. Anderson, Sustainable Resolutions for Environmental Threat of the Acid Mine Drainage, *Sci. Total Environ.*, 2020, **717**, 137211, DOI: **10.1016/j.scitotenv.2020.137211**.

14 A. B. Botelho Junior, D. B. Dreisinger and D. C. R. Espinosa, A Review of Nickel, Copper, and Cobalt Recovery by Chelating Ion Exchange Resins from Mining Processes and Mining Tailings, *Min. Metall. Explor.*, 2019, **36**(1), 199–213, DOI: **10.1007/s42461-018-0016-8**.

15 S. K. Sarker, N. Haque, M. Bhuiyan, W. Bruckard and B. K. Pramanik, Recovery of Strategically Important Critical Minerals from Mine Tailings, *J. Environ. Chem. Eng.*, 2022, **10**(3), 107622, DOI: **10.1016/j.jece.2022.107622**.

16 C. P. Kilmartin, J. A. Ouimet, A. W. Dowling and W. A. Phillip, Staged Diafiltration Cascades Provide Opportunities to Execute Highly Selective Separations, *Ind. Eng. Chem. Res.*, 2021, **60**(43), 15706–15719, DOI: **10.1021/acs.iecr.1c02984**.

17 Y. Zhang, N. E. Almodovar-Arbelo, J. L. Weidman, D. S. Corti, B. W. Boudouris and W. A. Phillip, Fit-for-Purpose Block Polymer Membranes Molecularly Engineered for Water Treatment, *npj Clean Water*, 2018, **1**(1), 1–14, DOI: **10.1038/s41545-018-0002-1**.

18 E. A. Eugene, W. A. Phillip and A. W. Dowling, Data Science-Enabled Molecular-to-Systems Engineering for Sustainable Water Treatment, *Curr. Opin. Chem. Eng.*, 2019, **26**, 122–130, DOI: **10.1016/j.coche.2019.10.002**.

19 R. M. DuChanois, M. Heiranian, J. Yang, C. J. Porter, Q. Li, X. Zhang, R. Verduzco and M. Elimelech, Designing Polymeric Membranes with Coordination Chemistry for High-Precision Ion Separations, *Sci. Adv.*, 2022, **8**(9), eabm9436, DOI: **10.1126/sciadv.abm9436**.

20 E. L. Cussler, Membranes Which Pump, *AIChE J.*, 1971, **17**(6), 1300–1303, DOI: **10.1002/aic.690170607**.

21 F. Kubota, Y. Shimobori, Y. Koyanagi, K. Shimojo, N. Kamiya and M. Goto, Uphill Transport of Rare-Earth Metals through a Highly Stable Supported Liquid Membrane Based on an Ionic Liquid, *Anal. Sci.*, 2010, **26**(3), 289–290, DOI: **10.2116/analsci.26.289**.

22 S. A. Ansari, P. K. Mohapatra and V. K. Manchanda, Recovery of Actinides and Lanthanides from High-Level Waste Using Hollow-Fiber Supported Liquid Membrane with TODGA as the Carrier, *Ind. Eng. Chem. Res.*, 2009, **48**(18), 8605–8612, DOI: **10.1021/ie900265y**.

23 A. J. B. Kemperman, D. Bargeman, Th. V. D. Boomgaard and H. Strathmann, Stability of Supported Liquid Membranes: State of the Art, *Sep. Sci. Technol.*, 1996, **31**(20), 2733–2762, DOI: **10.1080/01496399608000824**.

24 R. Epsztein, R. M. DuChanois, C. L. Ritt, A. Noy and M. Elimelech, Towards Single-Species Selectivity of Membranes with Subnanometre Pores, *Nat. Nanotechnol.*, 2020, **15**(6), 426–436, DOI: **10.1038/s41565-020-0713-6**.

25 R. Krishna and J. M. van Baten, Investigating the Relative Influences of Molecular Dimensions and Binding Energies on Diffusivities of Guest Species Inside Nanoporous Crystalline Materials, *J. Phys. Chem. C*, 2012, **116**(44), 23556–23568, DOI: **10.1021/jp308971w**.

26 N. A. Peppas and S. L. Wright, Drug Diffusion and Binding in Ionizable Interpenetrating Networks from Poly(Vinyl Alcohol) and Poly(Acrylic Acid), *Eur. J. Pharm. Biopharm.*, 1998, **46**(1), 15–29, DOI: **10.1016/S0939-6411(97)00113-6**.

27 L. X. Dang, Mechanism and Thermodynamics of Ion Selectivity in Aqueous Solutions of 18-Crown-6 Ether: A Molecular Dynamics Study, *J. Am. Chem. Soc.*, 1995, **117**(26), 6954–6960, DOI: **10.1021/ja00131a018**.

28 R. González-Pérez, S. Adams, A. W. Dowling, W. A. Phillip and J. Whitmer, Thermodynamics of Li+–Crown Ether Interactions in Aqueous Solvent, *ChemRxiv*, 2023, preprint, DOI: **10.26434/chemrxiv-2023-m0r2f**.

29 E. S. Zofchak, Z. Zhang, N. Marioni, T. J. Duncan, H. S. Sachar, A. Chamseddine, B. D. Freeman and V. Ganesan, Cation–Ligand Interactions Dictate Salt Partitioning and Diffusivity in Ligand-Functionalized Polymer Membranes, *Macromolecules*, 2022, **55**(6), 2260–2270, DOI: **10.1021/acs.macromol.2c00035**.

30 I. Sadeghi and A. Asatekin, Membranes with Functionalized Nanopores for Aromaticity-Based Separation of Small Molecules, *ACS Appl. Mater. Interfaces*, 2019, **11**(13), 12854–12862, DOI: **10.1021/acsami.9b00090**.

31 R. Sujanani, M. R. Landsman, S. Jiao, J. D. Moon, M. S. Shell, D. F. Lawler, L. E. Katz and B. D. Freeman, Designing Solute-Tailored Selectivity in Membranes: Perspectives for Water Reuse and Resource Recovery, *ACS Macro Lett.*, 2020, **9**(11), 1709–1717, DOI: **10.1021/acsmacrolett.0c00710**.

32 S. Benavides, S. Qu, F. Gao and W. A. Phillip, Polymeric Ion Pumps: Using an Oscillating Stimulus To Drive Solute Transport in Reactive Membranes, *Langmuir*, 2018, **34**(15), 4503–4514, DOI: **10.1021/acs.langmuir.8b00193**.

33 R. W. Baker, *Membrane Technology and Applications*, John Wiley & Sons, 2012.

34 C. Yang, E. E. Nuxoll and E. L. Cussler, Reactive Barrier Films, *AIChE J.*, 2001, **47**(2), 295–302, DOI: **10.1002/aic.690470208**.

35 T. Shimotori, E. L. Cussler and W. A. Arnold, Diffusion of Mobile Products in Reactive Barrier Membranes, *J. Membr. Sci.*, 2007, **291**(1), 111–119, DOI: **10.1016/j.memsci.2006.12.043**.

36 E. L. Cussler, R. Aris and A. Bhown, On the Limits of Facilitated Diffusion, *J. Membr. Sci.*, 1989, **43**(2), 149–164, DOI: **10.1016/S0376-7388(00)85094-2**.

37 S. Qu, T. Dilenschneider and W. A. Phillip, Preparation of Chemically-Tailored Copolymer Membranes with Tunable Ion Transport Properties, *ACS Appl. Mater. Interfaces*, 2015, **7**(35), 19746–19754, DOI: **10.1021/acsami.5b05592**.

38 Z. W. Muetzel, J. A. Ouimet and W. A. Phillip, Device for the Acquisition of Dynamic Data Enables the Rapid Characterization of Polymer Membranes, *ACS Appl. Polym. Mater.*, 2022, **4**(5), 3438–3447, DOI: **10.1021/acsapm.2c00048**.

39 J. L. Weidman, R. A. Mulvenna, B. W. Boudouris and W. A. Phillip, Nanostructured Membranes from Triblock Polymer Precursors as High Capacity Copper Adsorbents, *Langmuir*, 2015, **31**(40), 11113–11123, DOI: **10.1021/acs.langmuir.5b01605**.

40 J. Xu, C. Slykas, A. S. Braegelman, K. G. Alvarez, T. Kasl, B. W. Boudouris, M. J. Webber, V. Sharma and W. A. Phillip, Heavy Metal Removal Using Structured Sorbents 3D Printed from Carbon Nanotube-Enriched Polymer Solutions, *Matter*, 2022, **5**(10), 3432–3451, DOI: **10.1016/j.matt.2022.07.012**.

41 Y. Zhang, J. R. Vallin, J. K. Sahoo, F. Gao, B. W. Boudouris, M. J. Webber and W. A. Phillip, High-Affinity Detection and Capture of Heavy Metal Contaminants Using Block Polymer Composite Membranes, *ACS Cent. Sci.*, 2018, **4**(12), 1697–1707, DOI: **10.1021/acscentsci.8b00690**.

42 N. Chitpong and S. M. Husson, Polyacid Functionalized Cellulose Nanofiber Membranes for Removal of Heavy Metals from Impaired Waters, *J. Membr. Sci.*, 2017, **523**, 418–429, DOI: **10.1016/j.memsci.2016.10.020**.

43 N. Chitpong and S. M. Husson, High-Capacity, Nanofiber-Based Ion-Exchange Membranes for the Selective Recovery of Heavy Metals from Impaired Waters, *Sep. Purif. Technol.*, 2017, **179**, 94–103, DOI: **10.1016/j.seppur.2017.02.009**.

44 S. Wijeratne, M. L. Bruening and G. L. Baker, Layer-by-Layer Assembly of Thick, Cu2+-Chelating Films, *Langmuir*, 2013, **29**(41), 12720–12729, DOI: **10.1021/la402633x**.

45 H. Zhang, X. Hou, L. Zeng, F. Yang, L. Li, D. Yan, Y. Tian and L. Jiang, Bioinspired Artificial Single Ion Pump, *J. Am. Chem. Soc.*, 2013, **135**(43), 16102–16110, DOI: **10.1021/ja4037669**.

46 N. Liu, D. R. Dunphy, P. Atanassov, S. D. Bunge, Z. Chen, G. P. López, T. J. Boyle and C. J. Brinker, Photoregulation of Mass Transport through a Photoresponsive Azobenzene-Modified Nanoporous Membrane, *Nano Lett.*, 2004, **4**(4), 551–554, DOI: **10.1021/nl0350783**.

47 V. Singh Rathee, S. Qu, W. A. Phillip and J. K. Whitmer, A Coarse-Grained Thermodynamic Model for the Predictive Engineering of Valence-Selective Membranes, *Mol. Syst. Des. Eng.*, 2016, **1**(3), 301–312, DOI: **10.1039/C6ME00045B**.

48 S. P. Nunes, A. R. Behzad, B. Hooghan, R. Sougrat, M. Karunakaran, N. Pradeep, U. Vainio and K.-V. Peinemann, Switchable PH-Responsive Polymeric Membranes Prepared via Block Copolymer Micelle Assembly, *ACS Nano*, 2011, **5**(5), 3516–3522, DOI: **10.1021/nn200484v**.

49 S. Angelos, Y.-W. Yang, N. M. Khashab, J. F. Stoddart and J. I. Zink, Dual-Controlled Nanoparticles Exhibiting AND Logic, *J. Am. Chem. Soc.*, 2009, **131**(32), 11344–11346, DOI: **10.1021/ja9042752**.

50 M. J. Webber and M. W. Tibbitt, Dynamic and Reconfigurable Materials from Reversible Network Interactions, *Nat. Rev. Mater.*, 2022, **7**(7), 541–556, DOI: **10.1038/s41578-021-00412-x**.

51 J. A. Ouimet, J. Xu, C. Flores-Hansen, W. A. Phillip and B. W. Boudouris, Design Considerations for Next-Generation Polymer Sorbents: From Polymer Chemistry to Device Configurations, *Macromol. Chem. Phys.*, 2022, **223**(16), 2200032, DOI: **10.1002/macp.202200032**.

52 H. Vapnik, J. Elbert and X. Su, Redox-Copolymers for the Recovery of Rare Earth Elements by Electrochemically Regenerated Ion-Exchange, *J. Mater. Chem. A*, 2021, **9**(35), 20068–20077, DOI: **10.1039/D1TA03334D**.